

pubs.acs.org/acscatalysis Research Article

Conflicting Roles of Coordination Number on Catalytic Performance of Single-Atom Pt Catalysts

Dahong Huang, Ning He, Qianhong Zhu, Chiheng Chu, Seunghyun Weon, Kali Rigby, Xuechen Zhou, Lei Xu, Junfeng Niu,* Eli Stavitski, and Jae-Hong Kim*



Cite This: ACS Catal. 2021, 11, 5586-5592



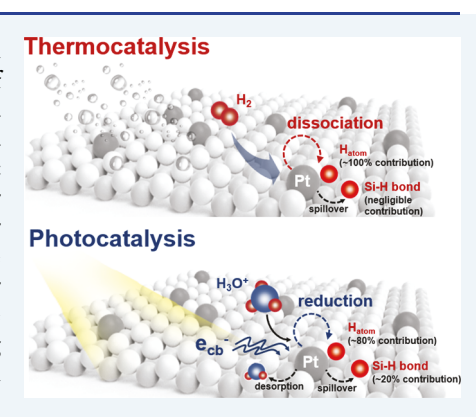
ACCESS

III Metrics & More

Article Recommendations

Supporting Information

ABSTRACT: Tailoring the coordination number (CN) of metal atoms has been increasingly recognized as one of the strategies to enhance the catalytic performance of single-atom catalysts (SACs). We here present the single-atom Pt loaded onto a semiconductor SiC substrate (Pt₁/SiC) with a high loading of up to 9.6 wt % and a precise control of its CN from 3 to 5. The CN tuning was enabled by binding organic linkers on the substrate surface and retaining the metal-linker bonds after photoreduction and mild thermal treatment from 80 to 160 °C. At a higher temperature, Pt became coordinated with additional oxygen atoms from the surface Si–OH groups and organic linkers. This resulted in the increase of the CN from 3 for Pt₁ treated at 80 °C to 5 at 160 °C. The Pt₁/SiCs with varying CNs effectively broke C–Br bonds in the model brominated compounds through both thermocatalysis using H₂ and photocatalysis using H⁺ as the source for strongly reducing atomic hydrogen (H_{atom}). The thermocatalytic debromination kinetics increased with the decreasing CN. However, photocatalytic debromination kinetics were independent of the CN,



contradictory to the prevalent understanding in literature. We attribute the differential CN effects on these two catalytic schemes to the differences in the pathways for the formation of H_{atom} as well as the rate-limiting step of the overall reaction pathways. Our study presents a unique and important example as to how the performance of SACs and the role of CN can significantly vary depending on the catalytic schemes.

KEYWORDS: coordination number, thermocatalysis, photocatalysis, single-atom catalysts, hydrodebromination

he last decade has witnessed the rapid development of single-atom catalysts (SACs), which demonstrate superior catalytic performance toward various important reactions, including CO oxidation, hydrogen production, and chemical synthesis.^{3,4} SACs achieve maximum atomic efficiency^{5,6} because each atom is accessible for the reaction, unlike catalysts in nanoscale cluster forms. SACs are designed to be strongly bound to the support material to overcome high surface free energies of individual exposed atoms and prevent their potential aggregation. 7,8 Such strong metal-support interaction additionally enables the facile manipulation of the coordination environment. 9-11 The significant influence of the identity of coordination atoms on the catalytic activity and selectivity of SACs has been extensively studied. 12-14 The relationship between the coordination number (CN) and catalytic performance is believed to be another critical factor for the design of SAC architectures. 15-17

In recent years, there has been growing interest in optimizing the catalytic performance of SACs by precisely engineering the CN. ^{18–20} In 2016, Li et al. first reported that single-atom Co displayed higher activity toward the oxygen reduction reaction as the CN of the Co-N shell decreased from 4 to 2. ¹⁷ This finding promoted further studies on the effect of

CN: for example, single-atom Pt exhibited increased reactivity for 3-nitrostyrene hydrogenation as the CN of the Pt-N shell decreased from 4 to 2;15 two-coordinated Ni-N more effectively promoted electrocatalytic CO₂ reduction compared to the three- or four-coordinated Ni-N shell; 19 a fivecoordinated Fe-N in Fe-N-C catalysts showed superior activity over Fe-N₆ and Fe-N₄ for the selective oxidation of C-H bonds.²¹ Recent findings collectively point toward a rather universal role of the CN on the catalytic properties of SACs. However, with the knowledge till date, it is difficult to generalize that the CN of SAC will affect all catalytic reactions, given a vastly large variation on the catalytic schemes for which SACs can be utilized. All reported studies so far focused on the thermocatalysis (e.g., hydrogenation by H_2^{15} and selective oxidation²¹) and electrocatalysis (e.g., CO₂ reduction, ^{20,22} O₂ reduction, 17,23 and H₂ evolution 16). We note that the CN

Received: February 9, 2021 Revised: April 7, 2021



effect on photocatalysis, another important application field for SACs, remains unknown.

It is noteworthy that most of these studies used hightemperature pyrolysis (≥ 500 °C), wherein the CN changed depending on the pyrolysis temperature during the thermal decomposition of selected metal-organic complex precursors under inert atmospheric conditions (i.e., Ar^{18-20} and $N_2^{17,21}$). However, this top-down synthetic strategy generally restricts the support to be a nitrogen-carbon material and suits only metal-nitrogen-carbon-based (M-N-C) SACs. Recently, Ren et al. reported a two-step method to overcome this limitation using ethanediamine as a ligand to chelate Pt cations and subsequently removing the ligand by a rapid thermal treatment under He atmosphere. 15 This work first demonstrated the CN regulation of SACs on Fe₂O₃, expanding the investigation of the CN effect to a new type of support. However, only a low metal loading (~1 wt %) could be achieved due to the inevitable metal migration and aggregation during the ligand removal process. 13,24 It is therefore critical to develop a generalized approach to regulate the CN of SACs at a high loading (≥5 wt %) on various supports.

Here, we synthesized atomically dispersed Pt catalysts with different CNs at a high metal loading (up to 9.6 wt %) via a simple wet chemical method using organic anchor-site linkers, UV irradiation, and thermal treatment in sequence. We finely regulated the CN of single-atom Pt by adjusting the thermal treatment temperature. A relatively low temperature (≤160 °C) was adopted to retain organic linkers and avoid Pt₁ aggregation during thermal treatment. We explored the CN effect on C-Br bond cleavage, a reaction of great interest in environmental remediation. Tetrabromobisphenol A (TBBPA), one of the most widely used brominated flame retardants, was chosen as the target compound due to its prevalence in the environment and potential human health risks. 25,26 TBBPA hydrodebromination via H₂-driven thermocatalysis was significantly affected by the CN effect, consistent with previous reports. In marked contrast, we first found that the photocatalytic pathway was barely influenced by the change in the CN. The relationship between catalytic performance and CN was investigated via detailed X-ray analyses, intermediate verifications, and theoretical calculations.

RESULTS AND DISCUSSION

Synthesis and Structural Characterization of Pt₁/SiC **SACs.** As shown in Figure 1a, a series of Pt₁/SiC samples were synthesized using a three-step process: surface modification of the SiC substrate (Step 1), photoreduction of H₂PtCl₆ into Pt₁ (Step 2), and thermal treatment to modulate the CN of Pt₁ (Step 3). The surface modification involved the reaction of surface Si-OH groups of SiC with (3-aminopropyl)trimethoxysilane (APTMS) (Figure 1b,c, and Figure S1). APTMS was chosen as the organic linker due to its ability to tune the electronic structure of metals²⁷ as well as the expectation that it could provide additional coordination with Pt₁ via Si-bound O, similar to the way Pt₁ binds to the surface Si-OH group. The addition of H₂PtCl₆ produced electrostatic interactions between the negatively charged Pt precursors (PtCl₆²⁻) and positively charged ammonium anchors on the APTMS-modified SiC. The Pt precursors were subsequently photoreduced to yield single-atom Pt₁/SiC (Figure S2). To control the CN of Pt1, we employed a low-temperature thermal treatment in air, from 80 to 160 °C for 60 min. Relatively mild

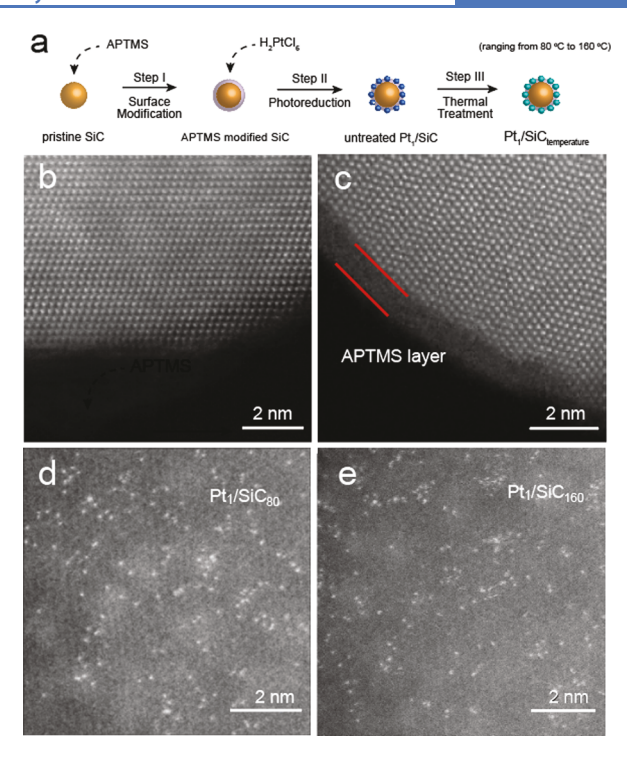


Figure 1. (a) Schematic illustration of the step-by-step synthesis procedure for Pt_1/SiC at different thermal treatment temperatures, labeled as $Pt_1/SiC_{temperature}$. Aberration-corrected high-angle annular dark-field scanning transmission electron microscopy (AC-HAADF-STEM) images of (b) pristine SiC, (c) APTMS-modified SiC substrate, (d) Pt_1/SiC_{80} , and (e) Pt_1/SiC_{160} .

conditions were applied to avoid the collapse of the APTMS ligand and enable the potential Pt_1 coordination with neighboring -OH groups from either surface Si-OH groups or adjacent -OH groups in the APTMS ligand.

The atomic dispersion of Pt₁ and the absence of Pt nanoparticles in Pt₁/SiC were visually confirmed by AC-HAADF-STEM images, as shown in Figure 1d,e and Figure S3. Thermal treatments up to 160 °C did not lead to the aggregation of Pt₁, nor the collapse of the APTMS layer (Figures S4 and S5). Further increasing the temperature to 180 °C resulted in the formation of Pt nanoparticles (Pt/SiC₁₈₀, Figure S3). Fourier-transformed extended X-ray absorption fine structure spectroscopy (FT-EXAFS, Figure 2a) confirmed the absence of Pt-Pt bonds and excluded the existence of Pt nanoparticles in samples below 160 °C, consistent with the results of AC-HAADF-STEM analysis. Comparison with a PtO₂ reference further demonstrated that the first coordination in Pt₁/SiC was a Pt-O shell. A small peak at 2.6 Å, similar to the Pt-O-Pt shell in PtO₂, is observed in all Pt₁/SiC catalysts, and we assign this peak to the second shell Pt1-Pt1 interaction.²⁸ While Pt atoms in Pt₁/SiC samples were all atomically dispersed and bound with oxygen atoms, they displayed distinctive features in Pt-O peak intensity. An increase in Pt-O peak intensity indicates higher Pt coordination with O and therefore an increase in the CN. Best-fit parameters extracted from FT-EXAFS data are summarized in Table 1. The average CN of Pt-O increased from 3.3 to 5.2, as thermal treatment temperature increased from 80 to 160 °C. Specifically, Pt₁/SiC₈₀, Pt₁/SiC₁₀₀, and Pt₁/ SiC₁₆₀ were identified as dominantly three-, four-, and fivecoordinated Pt₁/SiC, respectively. Optimized configurations of these Pt₁/SiC structures are presented in Figure S6.

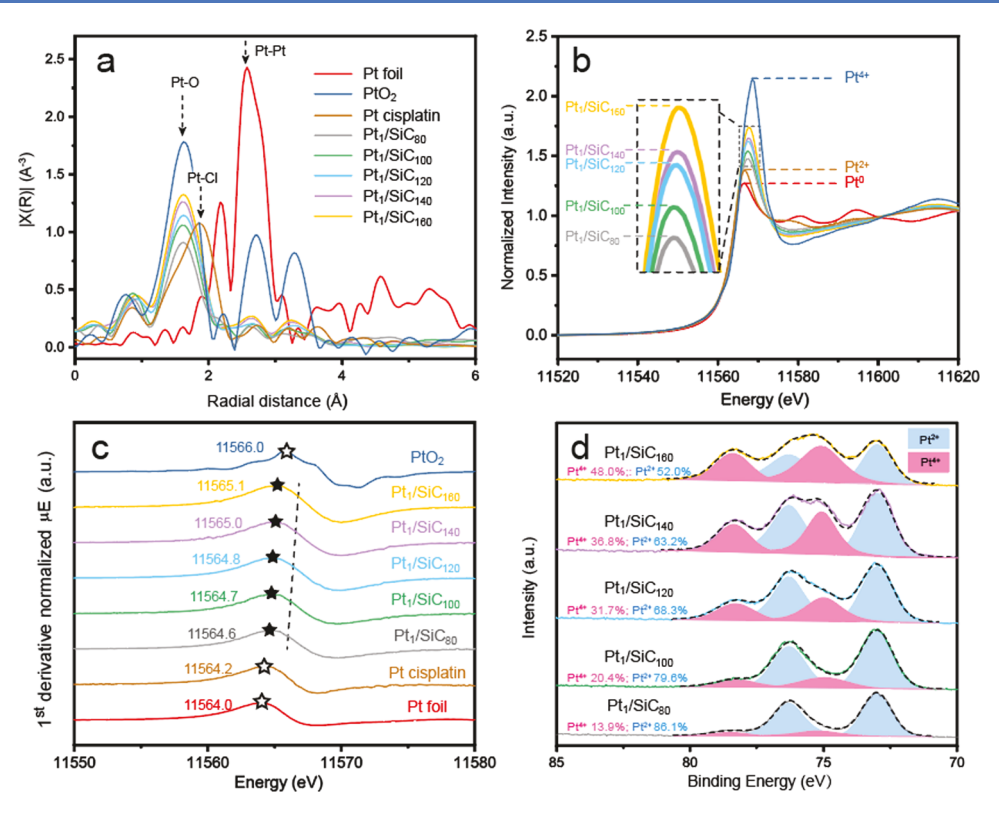


Figure 2. (a) Pt k^3 -weighted FT-EXAFS of Pt foil, PtO₂, Pt cisplatin ([Pt(NH₃)₂Cl₂]), and Pt₁/SiC_{temperature} samples; (b) normalized X-ray absorption near edge structure (XANES) measurements and (c) first derivative curves of different Pt₁/SiC_{temperature} samples and standards at the Pt L₃-edge; (d) Pt-4f X-ray photoelectron spectroscopy (XPS) spectra of Pt₁/SiC_{temperature} samples. The data ranges used for data fitting in K-space and R-space (Figure S7) were 3.0–10 Å⁻¹ and 1.2–2.5 Å, respectively.

Table 1. Best-Fit Structural Parameters Extracted from the Pt L_3 -edge FT-EXAFS Spectra of PtO₂ and Pt₁/SiC_{temperature} Samples^a

sample	shell	CN	R/Å	σ^2 / Å 2
Pt ₁ /SiC ₈₀	Pt-O	3.3 ± 0.4	2.01 ± 0.02	0.0054 ± 0.0019
Pt_1/SiC_{100}	Pt-O	3.9 ± 0.5	2.01 ± 0.01	0.0050 ± 0.0021
Pt_1/SiC_{120}	Pt-O	4.4 ± 0.6	2.02 ± 0.01	0.0054 ± 0.0025
Pt_1/SiC_{140}	Pt-O	4.6 ± 0.7	2.01 ± 0.01	0.0046 ± 0.0022
Pt_1/SiC_{160}	Pt-O	5.2 ± 0.6	2.02 ± 0.01	0.0056 ± 0.0025
PtO ₂	Pt-O	6	2.06	0.0010 ± 0.0007

^aCN is the coordination number of the Pt–O bond. R is the average interatomic distance between Pt and O atoms. σ^2 is the Debye–Waller factor, indicating the variance of the distance distribution.

As shown in Figure 2b,c, white line intensity and Pt peak position both qualitatively demonstrated that the oxidation state of Pt₁, positioned between Pt²⁺ and Pt⁴⁺, increased with increasing thermal treatment temperature. XPS analysis further corroborates this trend (Figure 2d). Spectral deconvolution (Pt²⁺ at 73.0 and 76.3 eV and Pt⁴⁺ at 75.1 and 78.4 eV)²⁹ suggested that the average oxidation states of Pt₁ are 2.28, 2.41, 2.63, 2.74, and 2.96 in Pt₁/SiC₈₀, Pt₁/SiC₁₀₀, Pt₁/SiC₁₂₀, Pt₁/SiC₁₄₀, and Pt₁/SiC₁₆₀, respectively. The results collectively indicated that both the oxidation state of Pt₁ and the CN of Pt-O bond linearly correlate with thermal treatment temperature, and there exists a linear relationship between the oxidation state and CN (Figure 3a).

We verified that Pt₁ was oxidized by the neighboring -OH groups, instead of O₂ in air, by preparing a series of control

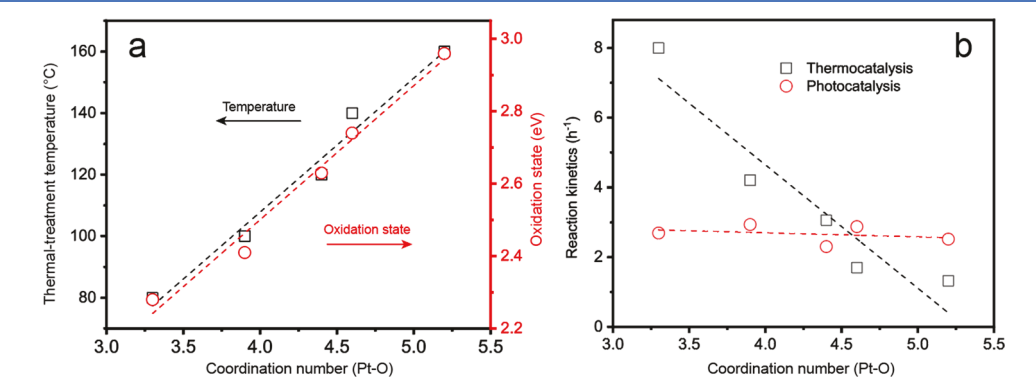


Figure 3. Correlation between (a) CN versus thermal treatment temperature (left y-axis) and oxidation state (right y-axis); and (b) CN and catalytic performance. Dashed lines represent linear regression.

samples via thermal treatment of Pt₁/SiC in N₂ atmosphere. Consistent with Pt₁/SiC obtained from the thermal treatment in air, XANES and FT-EXAFS data in Figure S8 showed that the oxidation state of Pt₁ also increased linearly with temperature. The overall reaction proceeds as Si-OH + Pt₁ $\rightarrow \frac{1}{2}$ H₂ + Si-O-Pt₁, ^{30,31} leading to the additional coordination in four- and five-coordinated Pt originating from the adjacent surface Si-OH groups and APTMS linker (Figure S7). This result marks the first instance of controlling the CN of SACs solely by coordination with the neighboring -OH groups. The significant Si-OH peak (532.6 eV in O-1s and 102.2 eV in Si-2p³²) and 27% atomic ratio of O atoms characterized by XPS analysis (Figure S9 and Table S1) demonstrated the high concentration of -OH groups in Pt₁/ SiC (i.e., before thermal treatment), which is an important prerequisite for the further oxidation of Pt1 by the aforementioned pathway.33,34

Relationship between the CN and Catalytic Performance. We investigated the relationship between the CN and catalytic performance by evaluating the thermocatalytic and photocatalytic activities of Pt₁/SiC_{temperature} catalysts for the activation of C-Br bonds in TBBPA. As shown in Figure 3b and Figure S10a, the kinetics of thermocatalysis (i.e., debromination under H₂-purging at room temperature) significantly increased as the CN decreased: first-order rate constant $k = 8.0 \text{ h}^{-1}$ for three-coordinated Pt₁/SiC₈₀, 4.2 h⁻¹ for four-coordinated Pt₁/SiC₁₀₀, and 1.3 h⁻¹ for fivecoordinated Pt₁/SiC₁₆₀. This observation is consistent with the previously reported studies, where the CN significantly affects the catalytic performance in both thermocatalytic and electrocatalytic systems. 15,17 However, in the photocatalytic system, we surprisingly and for the first time found that the CN had no influence on TBBPA degradation kinetics (~2.7 h⁻¹) (Figure 3b and Figure S10b). We attribute the disparate CN effects on thermocatalysis and photocatalysis to their differential reaction pathways.

Reaction Mechanisms. We first analyzed the reaction intermediates that formed during TBBPA debromination using Pt₁/SiC₈₀ as the representative catalyst (i.e., the material with the best catalytic performances in both catalyses). A series of partially debrominated intermediates [tri-, bi-, and monobrominated Bisphenol A (BPA)] and BPA (i.e., the final product) were detected by high performance liquid chromatography, demonstrating the occurrence of step-by-step hydrodebromination during both thermocatalysis and photocatalysis (Figure S11). Moreover, Pt₁/SiC₈₀ maintained high performance during recycling experiments (Figure S12) without aggregation or CN variation (Figure S13). A mass balance also confirmed that >95% TBBPA carbon was found as carbon in BPA after the completion of reaction, indicating a very high selectivity for TBBPA conversion into BPA in both catalytic schemes (Figure S14). However, there was a notable difference in bromine mass balance (Figure S14). Most Br atoms in TBBPA (~96%) became Br after thermocatalysis. In contrast, only ~80% Br atoms were found as Br ions in solution after the completion of TBBPA photocatalytic debromination. The emergence of the Si-Br peak in the XPS spectrum (Figure S15) indicated that the rest of the Br atoms became bound to the Si terminations on the SiC surface.

This difference might be related to the fact that reactive hydrogen species (H_{atom}) formed on Pt_1 through different pathways from different sources; that is, H_2 dissociation $(H_2 \rightarrow$

 $2~H_{atom}$) during thermocatalysis versus Volmer reaction (H⁺ + e⁻ \rightarrow H_{atom}) during photocatalysis. H_{atom} is a strong reductant and therefore readily replaces Br that is bound to carbon, releasing Br⁻ as the main product. This hydrodebromination appears to be the predominant pathway in thermocatalysis because the majority of Br in TBBPA ended up as Br⁻.

In the case of photocatalysis, an alternative hydrodebromination pathway should be involved. It is noted that H_{atom} can also desorb from Pt1 onto the Si terminations due to the low desorption energy and consequently form reactive Si-H bonds. 35,36 These Si-H bonds can lead to the abstraction of bromine atoms from TBBPA through atomic redistribution of Si-H/C-Br into Si-Br/C-H. Given that (1) Si-Br (310 kJ/ mol) is a stronger bond than C-Br (285 kJ/mol) and (2) C-H (411 kJ/mol) is a stronger bond than Si-H (318 kJ/mol), this redistribution is a thermodynamically favorable process (by ~118 kJ/mol). Previous studies have reported similar observations with hydrodefluorination, 37,38 which can be driven exclusively by Si-H bonds (Si-H/C-F conversion into Si-F/C-H) not by other pathways due to the high bond energy of C-F bonds (565 kJ/mol). The relatively low bond energy of C-Br enables additional hydrodebromination by free H_{atom} via the nucleophilic substitution, releasing Br⁻ into solution. The bromine mass balance during photocatalysis suggests that the ratio of C-Br bonds activated by free Hatom versus by Si-H bonds is about 80:20.

Two pathways for TBBPA hydrodebromation are schematically illustrated in Figure S16. In the case of thermocatalysis, where abundant H_{atom} are generated from H₂ dissociation, the reaction proceeds primarily through the direct nucleophilic H_{atom} attack on the electrophilic C atoms in C-Br bonds and the subsequent release of Br-. This pathway is likely much more kinetically favorable than the photocatalyic pathway involving Si-H bonds, which results from the heterolytic H₂ dissociation. 39,40 This hypothesis is evidenced by the observation that the reaction rate of thermocatalysis was ~2 times higher than that of photocatalysis. In the case of photocatalysis, Si-H bonds contribute to the overall kinetics because the H_{atom} pathway does not completely dominate the debromination pathway. However, the participation of the Si-H involving pathway is still relatively minor. The dominant pathway (~96% in thermocatalysis and ~80% in photocatalysis) involves H_{atom}, indicating that the differential CN effect is more likely to be influenced by the differences in the way Hatom forms.

We therefore performed density functional theory (DFT) simulation to examine how Hatom differently forms on Pt1 with different CNs during thermocatalysis and photocatalysis. We determined the lowest-energy pathway for thermocatalytic reaction as follows: (1) H₂O desorption from Pt₁, (2) H₂ adsorption onto Pt₁, and (3) H₂ dissociation on Pt₁ to form 2 H_{atom} (Figure 4). Our calculation suggested that the ratelimiting step would be H₂O desorption for three-coordinated Pt₁ (0.98 eV) and four-coordinated Pt₁ (1.12 eV), while it would be H_2 activation for five-coordinated Pt_1 (1.41 eV). This trend in the energy barrier is consistent with our experimental observation that the kinetics of thermocatalysis was in the order of three-coordinated Pt₁ > four-coordinated Pt₁ > fivecoordinated Pt₁. Note that the activation energy for the thermocatalysis with Pt₁/SiC₈₀ (i.e., three-coordinated Pt₁), obtained from another set of experiments performed with varying reaction temperatures (Figure S17), was 90.46 ± 9.8

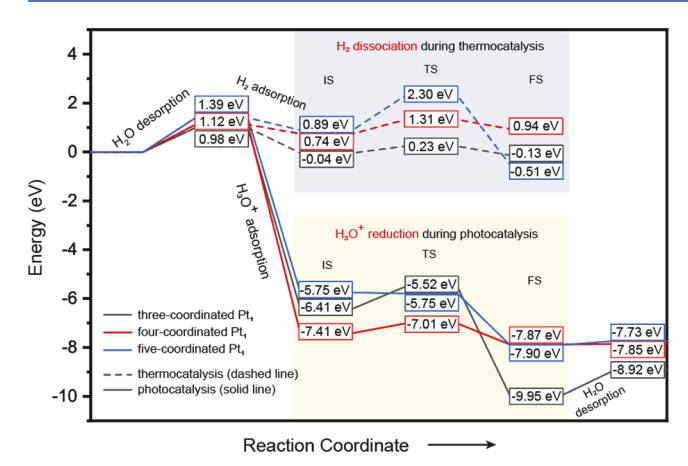


Figure 4. Density functional theory (DFT) calculated minimum energy paths of two catalytic reactions, thermocatalysis (dashed lines), and photocatalysis (solid lines), with three-coordinated Pt_1/SiC_{80} (black line), four-coordinated Pt_1/SiC_{100} (red line), and five-coordinated Pt_1/SiC_{160} (blue line). The gray box indicates H_2 dissociation during thermocatalysis, and the yellow box indicates H_3O^+ reduction during photocatalysis. IS stands for initial state, TS transition state, and FS final state. All theoretical models involved in the reaction process are presented in Figure S19.

kJ/mol (0.94 \pm 0.10 eV). This value is consistent with the energy barrier calculated by DFT (0.98 eV).

We also screened the reaction paths during photocatalysis and established the following reaction sequence: (1) H₂O desorption from Pt₁, (2) H₃O⁺ adsorption onto Pt₁, (3) H₃O⁺ reduction on Pt₁, and (4) H₂O desorption from Pt₁. These calculations suggest that the rate-limiting step among this sequence of steps should be H₂O desorption for threecoordinated Pt₁ (1.03 eV), four-coordinated Pt₁ (1.12 eV), and five-coordinated Pt₁ (1.39 eV). However, this simulation result would be inconsistent with our experimental results (i.e., that the kinetics did not vary depending on CN), if H₂O desorption were the limiting step for the overall reaction. The lack of temperature dependence of the photocatalytic kinetics (Figure S18a) assured that H₂O desorption is not the rate-limiting step. This observation strongly suggests that photoexcitation of SiC and generation of excitons, which are known to be temperature-independent, determines the overall kinetics. This photoexcitation process is dependent only on the semiconductor substrate SiC, explaining why the overall kinetics were independent of the CN of Pt₁.

There exist a growing number of reports and an increasingly prevalent notion that the CN of metal atoms affects the reactivity and selectivity of catalytic reactions driven by SACs. We observed that the kinetics of TBBPA hydrodebromination via thermocatalysis indeed linearly correlated with the CN, with faster rates observed with lower coordinated Pt1. However, our results also present an important contradicting example. The kinetics of photocatalytic hydrodebromination of TBBPA were independent of the CN of Pt₁ because reaction steps involving Pt₁ were not rate-limiting, despite the dependency on the CN. Overall slower kinetics in photocatalysis is attributed to the insufficient H_{atom} formation, resulting in the involvement of atomic redistribution of Si-H/ C-Br (into Si-Br/C-H). Our study highlights the importance of the substrate that anchors SACs, wherein the substrate plays a key role in the overall reaction kinetics. It also calls for further research in establishing a comprehensive

understanding of the CN effects on catalytic performance using SACs with well-defined CNs as well as high metal loading and various supports, as demonstrated in our study.

ASSOCIATED CONTENT

Supporting Information

The Supporting Information is available free of charge at https://pubs.acs.org/doi/10.1021/acscatal.1c00627.

Calculations of the density of Pt atoms, materials, details of the catalyst preparation, assessments of photocatalytic and thermocatalytic performances, DFT computational details; supplementary characterizations with XPS, AC-HAADF-STEM, X-ray powder diffraction, high-resolution transmission electron microscopy, XAFS; photocatalytic and thermocatalytic kinetics, recycling experiments, carbon and bromine mass balances, HPLC spectrums, energy profiles for hydrodebromination, Arrhenius plot for the calculation of apparent activation energy, optimized structures involved in two catalyses (PDF)

AUTHOR INFORMATION

Corresponding Authors

Junfeng Niu — School of Environment and Civil Engineering, Dongguan University of Technology, Dongguan, Guangdong 523808, P.R. China; ⊚ orcid.org/0000-0003-2592-3103; Phone: +86-769-22863180; Email: niujf@dgut.edu.cn

Jae-Hong Kim — Department of Chemical and Environmental Engineering, Yale University, New Haven, Connecticut 06520, United States; ⊚ orcid.org/0000-0003-2224-3516; Phone: +1-203-432-4386; Email: jaehong.kim@yale.edu; Fax: +1-203-432-4387

Authors

Dahong Huang — School of Environment and Civil Engineering, Dongguan University of Technology, Dongguan, Guangdong 523808, P.R. China; Department of Chemical and Environmental Engineering, Yale University, New Haven, Connecticut 06520, United States; orcid.org/0000-0003-4544-6113

Ning He – School of Chemical Engineering, Dalian University of Technology, Dalian 116024, P.R. China

Qianhong Zhu — Department of Chemical and Environmental Engineering, Yale University, New Haven, Connecticut 06520, United States

Chiheng Chu — Department of Chemical and Environmental Engineering, Yale University, New Haven, Connecticut 06520, United States; orcid.org/0000-0001-9493-9120

Seunghyun Weon — School of Health and Environmental Science, Korea University, Seoul 02841, Korea; orcid.org/0000-0003-4529-8069

Kali Rigby — Department of Chemical and Environmental Engineering, Yale University, New Haven, Connecticut 06520, United States; orcid.org/0000-0002-4582-2388

Xuechen Zhou – Department of Chemical and Environmental Engineering, Yale University, New Haven, Connecticut 06520, United States

Lei Xu – School of Environment and Civil Engineering, Dongguan University of Technology, Dongguan, Guangdong 523808, P.R. China Eli Stavitski – National Synchrotron Light Source- II, Brookhaven National Laboratory, Upton, New York 11973, United States

Complete contact information is available at: https://pubs.acs.org/10.1021/acscatal.1c00627

Notes

The authors declare no competing financial interest.

ACKNOWLEDGMENTS

This study was financially supported by the National Science Fund for Distinguished Young Scholars (No. 51625801), the National Natural Science Foundation of China (No. 51878169), the Guangdong Innovation Team Project for Colleges and Universities (No. 2016KCXTD023), and Guangdong Province Universities and Colleges Pearl River Scholar Funded Scheme (2017). This study was partly supported the National Science Foundation (NSF) Nanosystems Engineering Research Center for Nanotechnology-Enabled Water Treatment (EEC-1449500) and NSF Division of Chemical, Bioengineering, Environmental, and Transport Systems (CBET) Grant #1955793. This research used beamline 8-ID (Inner Shell Spectrscopy, ISS) of the National Synchrotron Light Source II, a U.S. Department of Energy (DOE) Office of Science User Facility operated for the DOE Office of Science by Brookhaven National Laboratory under Contract No. DE-SC0012704.

REFERENCES

- (1) Qiao, B.; Wang, A.; Yang, X.; Allard, L. F.; Jiang, Z.; Cui, Y.; Liu, J.; Li, J.; Zhang, T. Single-Atom Catalysis of CO Oxidation using Pt₁/FeO_x. Nat. Chem. **2011**, *3*, 634–641.
- (2) Cheng, N.; Stambula, S.; Wang, D.; Banis, M. N.; Liu, J.; Riese, A.; Xiao, B.; Li, R.; Sham, T.-K.; Liu, L.-M. Platinum Single-Atom and Cluster Catalysis of the Hydrogen Evolution Reaction. *Nat. Commun.* **2016**, *7*, No. 13638.
- (3) Harrath, K.; Yu, X.; Xiao, H.; Li, J. The Key Role of Support Surface Hydrogenation in the CH₄ to CH₃OH Selective Oxidation by a ZrO₂-supported Single-Atom Catalyst. *ACS Catal.* **2019**, *9*, 8903–8909
- (4) Lou, Y.; Zheng, Y.; Li, X.; Ta, N.; Xu, J.; Nie, Y.; Cho, K.; Liu, J. Pocketlike Active Site of $\mathrm{Rh_1/MoS_2}$ Single-Atom Catalyst for Selective Crotonaldehyde Hydrogenation. *J. Am. Chem. Soc.* **2019**, *141*, 19289–19295.
- (5) Wang, A.; Li, J.; Zhang, T. Heterogeneous Single-Atom Catalysis. *Nat. Rev. Chem.* **2018**, *2*, 65–81.
- (6) Rong, X.; Wang, H. J.; Lu, X. L.; Si, R.; Lu, T. B. Controlled Synthesis of a Vacancy-Defect Single-Atom Catalyst for Boosting CO₂ Electroreduction. *Angew. Chem., Int. Ed.* **2020**, *59*, 1961–1965.
- (7) Lin, J.; Wang, A.; Qiao, B.; Liu, X.; Yang, X.; Wang, X.; Liang, J.; Li, J.; Liu, J.; Zhang, T. Remarkable Performance of Ir₁/FeO_x Single-Atom Catalyst in Water Gas Shift Reaction. *J. Am. Chem. Soc.* **2013**, 135, 15314–15317.
- (8) Yan, H.; Cheng, H.; Yi, H.; Lin, Y.; Yao, T.; Wang, C.; Li, J.; Wei, S.; Lu, J. Single-atom $Pd_1/graphene$ catalyst Achieved by Atomic Layer Deposition: Remarkable Performance in Selective Hydrogenation of 1, 3-butadiene. *J. Am. Chem. Soc.* **2015**, *137*, 10484–10487.
- (9) Jakub, Z.; Hulva, J.; Meier, M.; Bliem, R.; Kraushofer, F.; Setvin, M.; Schmid, M.; Diebold, U.; Franchini, C.; Parkinson, G. S. Local Structure and Coordination Define Adsorption in a Model Ir₁/Fe₃O₄ Single-Atom Catalyst. *Angew. Chem., Int. Ed.* **2019**, *58*, 13961–13968.
- (10) Xiao, M.; Zhu, J.; Li, G.; Li, N.; Li, S.; Cano, Z. P.; Ma, L.; Cui, P.; Xu, P.; Jiang, G. A Single-Atom Iridium Heterogeneous Catalyst in Oxygen Reduction Reaction. *Angew. Chem., Int. Ed.* **2019**, *131*, 9742–9747.

- (11) Weon, S.; Huang, D.; Rigby, K.; Chu, C.; Wu, X.; Kim, J.-H. Environmental Materials beyond and below the Nanoscale: Single-Atom Catalysts. *ACS EST Eng.* **2021**, *1*, 157–172.
- (12) Lang, R.; Xi, W.; Liu, J.-C.; Cui, Y.-T.; Li, T.; Lee, A. F.; Chen, F.; Chen, Y.; Li, L.; Li, L. Non Defect-Stabilized Thermally Stable Single-atom Catalyst. *Nat. Commun.* **2019**, *10*, 234.
- (13) Li, J.; Chen, S.; Yang, N.; Deng, M.; Ibraheem, S.; Deng, J.; Li, J.; Li, L.; Wei, Z. Ultrahigh-Loading Zinc Single-Atom Catalyst for Highly Efficient Oxygen Reduction in Both Acidic and Alkaline Media. *Angew. Chem., Int. Ed.* **2019**, 58, 7035–7039.
- (14) Ren, W.; Tan, X.; Yang, W.; Jia, C.; Xu, S.; Wang, K.; Smith, S. C.; Zhao, C. Isolated Diatomic Ni-Fe Metal—Nitrogen Sites for Synergistic Electroreduction of CO₂. *Angew. Chem., Int. Ed.* **2019**, 58, 6972–6976.
- (15) Ren, Y.; Tang, Y.; Zhang, L.; Liu, X.; Li, L.; Miao, S.; Sheng Su, D.; Wang, A.; Li, J.; Zhang, T. Unraveling the Coordination Structure-Performance Relationship in Pt_1/Fe_2O_3 Single-Atom Catalyst. *Nat. Commun.* **2019**, *10*, 4500.
- (16) Yin, X. P.; Wang, H. J.; Tang, S. F.; Lu, X. L.; Shu, M.; Si, R.; Lu, T. B. Engineering the Coordination Environment of Single-Atom Pt Anchored on Graphdiyne for Optimizing Electrocatalytic Hydrogen Evolution. *Angew. Chem., Int. Ed.* **2018**, *57*, 9382–9386.
- (17) Yin, P.; Yao, T.; Wu, Y.; Zheng, L.; Lin, Y.; Liu, W.; Ju, H.; Zhu, J.; Hong, X.; Deng, Z.; Zhou, G.; Wei, S.; Li, Y. Single Cobalt Atoms with Precise N-Coordination as Superior Oxygen Reduction Reaction Catalysts. *Angew. Chem., Int. Ed.* **2016**, *128*, 10958–10963.
- (18) Pan, Y.; Chen, Y.; Wu, K.; Chen, Z.; Liu, S.; Cao, X.; Cheong, W. C.; Meng, T.; Luo, J.; Zheng, L.; Liu, C.; Wang, D.; Peng, Q.; Li, J.; Chen, C. Regulating the Coordination Structure of Single-Atom Fe-N_xC_y Catalytic Sites for Benzene Oxidation. *Nat. Commun.* **2019**, *10*, 4290.
- (19) Gong, Y. N.; Jiao, L.; Qian, Y.; Pan, C. Y.; Zheng, L.; Cai, X.; Liu, B.; Yu, S. H.; Jiang, H. L. Regulating the Coordination Environment of MOF-Templated Single-Atom Nickel Electrocatalysts for Boosting ${\rm CO_2}$ Reduction. *Angew. Chem., Int. Ed.* **2020**, *59*, 2705–2709.
- (20) Wang, X.; Chen, Z.; Zhao, X.; Yao, T.; Chen, W.; You, R.; Zhao, C.; Wu, G.; Wang, J.; Huang, W.; Yang, J.; Hong, X.; Wei, S.; Wu, Y.; Li, Y. Regulation of Coordination Number over Single Co Sites: Triggering the Efficient Electroreduction of CO₂. Angew. Chem., Int. Ed. 2018, 57, 1944–1948.
- (21) Liu, W.; Zhang, L.; Liu, X.; Liu, X.; Yang, X.; Miao, S.; Wang, W.; Wang, A.; Zhang, T. Discriminating Catalytically Active FeN_x Species of Atomically Dispersed Fe-N-C Catalyst for Selective Oxidation of the C-H Bond. *J. Am. Chem. Soc.* **2017**, *139*, 10790–10798.
- (22) Zhang, H.; Li, J.; Xi, S.; Du, Y.; Hai, X.; Wang, J.; Xu, H.; Wu, G.; Zhang, J.; Lu, J.; Wang, J. A Graphene-Supported Single-Atom FeN_5 Catalytic Site for Efficient Electrochemical CO_2 Reduction. *Angew. Chem., Int. Ed.* **2019**, *58*, 14871–14876.
- (23) Tang, C.; Jiao, Y.; Shi, B.; Liu, J. N.; Xie, Z.; Chen, X.; Zhang, Q.; Qiao, S.-Z. Coordination Tunes Selectivity: Two-Electron Oxygen Reduction on High-Loading Molybdenum Single-Atom Catalysts. *Angew. Chem., Int. Ed.* **2020**, 132, 9256–9261.
- (24) Zhao, L.; Zhang, Y.; Huang, L.-B.; Liu, X.-Z.; Zhang, Q.-H.; He, C.; Wu, Z.-Y.; Zhang, L.-J.; Wu, J.; Yang, W. Cascade Anchoring Strategy for General Mass Production of High-loading Single-atomic Metal-nitrogen Catalysts. *Nat. Commun.* **2019**, *10*, 1278.
- (25) Ding, Y.; Zhu, L.; Wang, N.; Tang, H. Sulfate Radicals Induced Degradation of Tetrabromobisphenol A with Nanoscaled Magnetic CuFe₂O₄ as a Heterogeneous Catalyst of Peroxymonosulfate. *Appl. Catal. B* **2013**, *129*, 153–162.
- (26) Gu, C.; Wang, J.; Liu, S.; Liu, G.; Lu, H.; Jin, R. Biogenic Fenton-like Reaction Involvement in Cometabolic Degradation of Tetrabromobisphenol A by Pseudomonas sp. fz. *Environ. Sci. Technol.* **2016**, *50*, 9981–9989.
- (27) Chu, C.; Huang, D.; Zhu, Q.; Stavitski, E.; Spies, J. A.; Pan, Z.; Mao, J.; Xin, H. L.; Schmuttenmaer, C. A.; Hu, S.; Kim, J.-H. Electronic Tuning of Metal Nanoparticles for Highly Efficient

- Photocatalytic Hydrogen Peroxide Production. ACS Catal. 2019, 9, 626–631.
- (28) Bai, L.; Hsu, C.-S.; Alexander, D. T. L.; Chen, H. M.; Hu, X. A Cobalt-Iron Double-Atom Catalyst for the Oxygen Evolution Reaction. J. Am. Chem. Soc. 2019, 141, 14190-14199.
- (29) Godoi, D. R. M.; Perez, J.; Villullas, H. M. Alloys and Oxides on Carbon-supported Pt-Sn Electrocatalysts for Ethanol Oxidation. *J. Power Sources* **2010**, *195*, 3394–3401.
- (30) Sanz, J. F.; Hernandez, N. C. Mechanism of Cu Deposition on the Alpha-Al₂O₃ (0001) Surface. *Phys. Rev. Lett.* **2005**, 94, No. 016104.
- (31) Chambers, S.; Droubay, T.; Jennison, D. R.; Mattsson, T. Laminar Growth of Ultrathin Metal Films on Metal Oxides: Co on Hydroxylated α -Al₂O₃ (0001). *Science* **2002**, 297, 827–831.
- (32) Peng, Y.; Wang, L.; Luo, Q.; Cao, Y.; Dai, Y.; Li, Z.; Li, H.; Zheng, X.; Yan, W.; Yang, J. Molecular-level Insight into How Hydroxyl Groups Boost Catalytic Activity in CO₂ Hydrogenation into Methanol. *Chem* **2018**, *4*, 613–625.
- (33) Brown, M. A.; Fujimori, Y.; Ringleb, F.; Shao, X.; Stavale, F.; Nilius, N.; Sterrer, M.; Freund, H.-J. Oxidation of Au by Surface OH: Nucleation and Electronic Structure of Gold on Hydroxylated MgO (001). J. Am. Chem. Soc. 2011, 133, 10668–10676.
- (34) Fujimori, Y.; Kaden, W. E.; Brown, M. A.; Roldan Cuenya, B.; Sterrer, M.; Freund, H.-J. Hydrogen Evolution from Metal—Surface Hydroxyl Interaction. *J. Phys. Chem. C* **2014**, *118*, 17717—17723.
- (35) Huang, D.; de Vera, G. A.; Chu, C.; Zhu, Q.; Stavitski, E.; Mao, J.; Xin, H.; Spies, J. A.; Schmuttenmaer, C. A.; Niu, J. Single-atom Pt Catalyst for Effective C–F bond activation via Hydrodefluorination. *ACS Catal.* **2018**, *8*, 9353–9358.
- (36) Lucci, F. R.; Liu, J.; Marcinkowski, M. D.; Yang, M.; Allard, L. F.; Flytzani-Stephanopoulos, M.; Sykes, E. C. H. Selective Hydrogenation of 1, 3-butadiene on Platinum—copper ALloys at the Singleatom Limit. *Nat. Commun.* **2015**, *6*, 8550.
- (37) Douvris, C.; Ozerov, O. V. Hydrodefluorination of Perfluoroalkyl Groups using Silylium-carborane Catalysts. *Science* **2008**, 321, 1188–1190.
- (38) Scott, V. J.; Çelenligil-Çetin, R.; Ozerov, O. V. Room-temperature Catalytic Hydrodefluorination of C (sp³)–F bonds. *J. Am. Chem. Soc.* **2005**, *127*, 2852–2853.
- (39) Zhang, L.; Zhou, M.; Wang, A.; Zhang, T. Selective Hydrogenation over Supported Metal Catalysts: from Nanoparticles to Single Atoms. *Chem. Rev.* **2020**, *120*, *683*–733.
- (40) Kuai, L.; Chen, Z.; Liu, S.; Kan, E.; Yu, N.; Ren, Y.; Fang, C.; Li, X.; Li, Y.; Geng, B. Titania Supported Synergistic Palladium Single Atoms and Nanoparticles for Room Temperature Ketone and Aldehydes Hydrogenation. *Nat. Commun.* **2020**, *11*, 1–9.